Jurnal Tribologi 23 (2019) 113-124

MYTRIBOS Malaysian Tribology Society

Jurnal Tribologi

Website : jurnaltribologi.mytribos.org e-issn: 2289-7232

Enhancing wear resistance using selective laser melting (SLM): Influence of scanning strategy

Yang Yang, Yi Zhu *, Huayong Yang

State Key Laboratory of Fluid Power and Mechatronic Systems, Zhejiang University, 38 Zheda Road, 310027 Hangzhou, CHINA.
*Corresponding author: yiz@zju.edu.cn

KEYWORDS

Selective laser melting
Scanning strategy
Wear resistance

ABSTRACT

In selective laser melting (SLM), process parameters, such as laser power, hatch space, and scanning speed, greatly affect part properties. Wear resistance is crucial for many functional parts, which is usually enhanced by post processing for SLMed parts. Those post processing are efficient but are not always accessible due to very complex structures or limited manufacturing time. Therefore, it is important to enhance the wear resistance during SLM process by actively control the microstructures. The paper studied the influence of scanning strategy on the microstructures and wear resistance. Three scanning strategies, "zigzag", parallel remelting, and perpendicular remelting, were used to fabricate 316L stainless steel samples using SLM. The microstructures of samples were characterized and the hardness was measured. The scratch depths under 1, 3, and 5 N were measured and the scratch track morphologies were examined. Results indicate that the hardness and wear resistance can be enhanced by using remelting due to the refined microstructures resulted from remelting. The part produced using perpendicular remelting strategy has the highest hardness and the lowest scratch depth due to a fiber texture.

Received 25 September 2019; received in revised form 13 November 2019; accepted 2 December 2019.
To cite this article: Yang et al. (2019). Enhancing wear resistance using selective laser melting (SLM): Influence of scanning strategy. Jurnal Tribologi 23, pp.113-124.

1.0 INTRODUCTION

Selective laser melting (SLM) is one of the most widely used additive manufacturing technologies to fabricate metal parts. In the SLM process, a high energy laser melts metal powders layer by layer according to the sliced model file. Compared to the conventional processes (CP) such as casting and forging, SLM is particularly suitable for fabricating parts with high degree of geometrical and functional complexity. However, the variation in microstructures is great due to complex heat transfer is SLM, which directly affects the part properties. Therefore, the process parameters – microstructures – properties relation becomes a hotspot in the research community.

The friction and wear performance of parts is crucial to the machine lifetime and reliability. The tribological behaviors of SLM-fabricated parts are different from those of the CP parts due to different microstructures (Zhu et al., 2016). Zhu et al. (2019) revealed the lubricating performance of the SS316L samples. It was found that a few small pores (porosity at or below 1%) produced in SLM process positively affect lubrication by providing local extra lubrication and serving as debris containers. The effects of microstructure on wear behaviors of the SLM fabricated SS316L samples under dry conditions were also studied by Yang et al. (2019). Severe damage was found in the Sz sliding direction after the scratch tests due to the slipping of columnar structures. Some studies focused on enhancing wear resistance by adding different particles (Lemke et al., 2018; Cai et al., 2019; Wen et al., 2018). However, research on the influence of the process parameters on the wear resistance are rare.

The SLM process parameters (see Figure 1) greatly affect the density, surface roughness, and mechanical properties. To date, many researchers has focused on studying the influence of the process parameters such as laser power (J H Yi et al., 2019), scanning speed (Choi et al., 2016; qiu et al., 2016), hatch space (Li et al., 2010), and scanning strategy, on various mechanical properties. The scanning strategy, determines the laser scan path on the metal powders, affects the heat flow, grain growth, and microstructure. Wan et al. (2019) used two scanning strategies including 0° and 90° rotation between layers to produce Inconel 718 samples. The results show the former has a higher tensile and fatigue strength compared with the latter. Carter et al. (2014) used the 'island' scanning strategy to fabricate the nickel superalloy CM247LC samples. A bimodal grain structure including columnar and fine-grained regions were observed. Moreover, cracks occur in the fine-grained boundary regions. Thijs et al. (2013) studied the effect of different scanning strategies on the microstructure and crystallographic texture of AlSi10Mg samples. A strong partial <100> along the scanning direction and a weak cubic texture around the build direction were found in samples produced using the 0° and 90° rotation strategies, respectively. However, little attention has been devoted to the influence of scanning strategies on the wear behaviors.

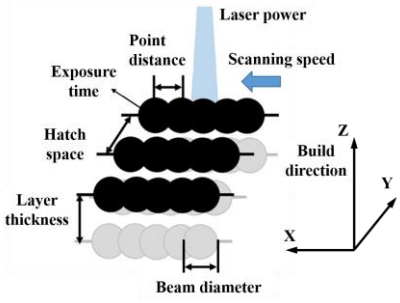

Figure 1: The SLM process parameters effect to the density.

In this study, the stainless steel 316L samples were fabricated by SLM using different remelting strategies. Scratch tests were performed under different loads. The microstructures and wear behaviors after scratch tests were analyzed.

2.0 EXPERIMENTAL DETAILS

2.1 Manufacture of Samples

The 316L stainless steel samples used in this study were fabricated using a Renishaw AM250 SLM system, which is equipped with an SPI redPOWER 200 W ytterbium fibre laser in a Q-switched mode. The laser operates with a 70 μm focused beam diameter at a 1071 nm wavelength. All samples were fabricated in a nitrogen environment to minimize oxidation in SLM process. The 316L stainless steel powder were purchased from Renishaw plc., which ranges from 15 to 45 μm with a spherical shape.

Table 1 Process parameters and scanning strategies of the 316 L stainless steel samples fabricated by SLM

Sample	Laser power (W)	Scanning speed (mm/s)	Hatch space (μm)	Layer thickness (μm)	Rotation between layers (°)	Energy density (J/mm³)	Scanning strategy
A	200	750	110	50	0	48	Zigzag
B	200	750	110	50	0	96	Parallel remelting
C	200	750	110	50	0	96	Perpendicular remelting

The cubic 316L stainless steel samples with the dimension of 10×10×10 mm3 were fabricated using the same process parameters provided by Renishaw plc. but different scanning strategies, as listed in Table 1. The energy density (J/mm3) was calculated according to the definition from (Zhu et al., 2018):

$$E = \frac{P}{h_s \times v \times l} \quad (1)$$

Where P is laser power (W), h_s is hatch space, v is scanning speed (mm/s) defined as the point distance divided by the exposure time, l is layer thickness.

Three samples were produced using three types of scanning strategies: regular "zigzag" without remelting (sample A); parallel remelting (sample B); and perpendicular remelting (sample C). In the regular "zigzag", the rotation angle of scanning between adjacent layers is 0°. As shown in Figure 2, the sample B was remelted using the same scanning vectors as the first melting while the sample C was remelted using the perpendicular scanning vectors after the first melting.

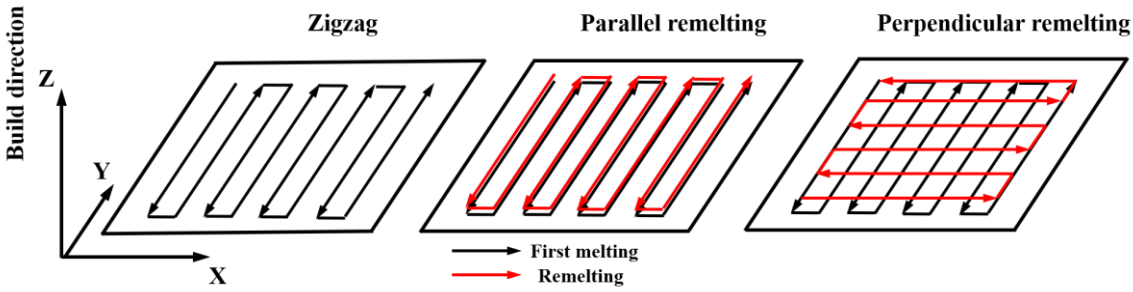

Figure 2: Sample remelting direction.

2.2 Material Characterization

The hardness measurements were conducted using a Vickers hardness tester with a 50 g load and 15 s dwell time. Before the hardness tests, all samples were polished using 320# SiC sandpaper and diamond suspensions (9 µm, 3 µm, and 1 µm) successively. The average hardness values were calculated according to ten measurements for each sample, which were made along the centre line on side surface of samples, as shown in Figure 3. The polished samples were etched using Glyceregia etchant (10 ml glycerine + 15 ml HCl + 5 ml HNO3) to examine the microstructures. The microstructures of samples were then observed using a confocal laser scanning microscope (CLSM; VK-X100 series Keyence Corp, Japan) and a scanning electron microscope (SEM; SU70 Hitachi Corp, Japan). Electron back scattered diffraction (EBSD) was used to investigate the grain and texture development in different samples. The scanning step is 1.5 µm for all EBSD experiments in this study.

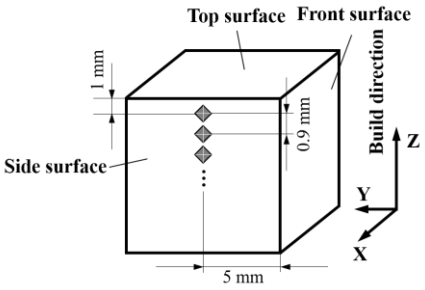

Figure 3: Location of hardness measurement.

2.3 Scratch Test

The single pass scratch tests were conducted using an automatic scratch tester (WS-2005, Lanzhou Zhongke Kaihua Technology Development Co., Ltd. China). The diamond indenter has a spherical tip with a radius of 200 µm and a core of 120°. The scratch was performed on the side surface for all samples with a constant sliding speed of 10 mm/min. The sliding direction is parallel to Z axis and the sliding distance is 5 mm. Different normal loads including 1 N, 3 N, and 5 N were applied. All samples were polished before the scratch tests.

3.0 RESULTS AND DISCUSSION

3.1 Microstructure

Figure 4 shows the layered microstructures on the side surface of the sample A, B, and C. The microstructures of the sample A and B are similar, which are both characterized by approximately horizontal molten tracks due to the same laser melting vectors in each layer. The crescent shape molten pools (indicated by red dotted lines) were found in the sample C caused by the perpendicular remelting. A higher magnification was used to examine detailed microstructure. As shown in Figure 5a-c, the typical columnar structures along with the build direction can be observed in all samples. It should be noted that the columnar structures in both the samples B and C are smaller than those in the sample A indicating refinement of microstructure occurred in remelting process (Yasa et al., 2011). Moreover, the columnar structures perpendicular to the build direction were found in the sample C (see Figure 5d), which grow through the molten pool boundary and are normal to the molten pool boundary. Comparing with the columnar structures, the cellular structures do not show noticeable difference between the samples A, B, and C (see Figure 5e, f, and g).

Figure 6 shows the EBSD images on the side surface of all three samples. In Figure 6a and b, a dominant alignment of the <001> direction with Z axis, i.e. the build direction was found indicating a fibre texture in the samples A and B. However, no dominant texture was observed in the sample C due to the weak alignment of the <001>, <101>, and <111> directions with different axes, as shown in Figure 6c. It indicates that the crystallographic texture was closely related to the scanning strategies. The change of the direction of remelting vectors in perpendicular remelting weakened the formation of fibre texture.

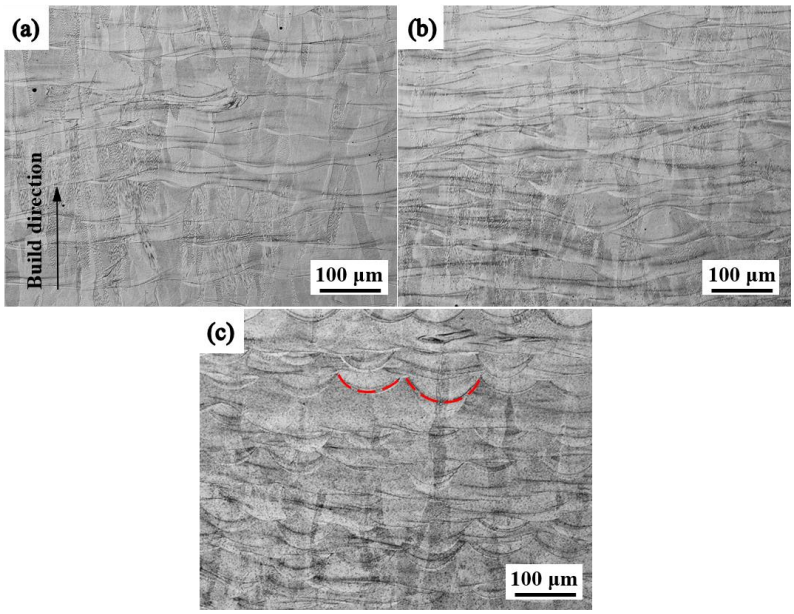

Figure 4: Microstructure layer for samples A, B, and C.

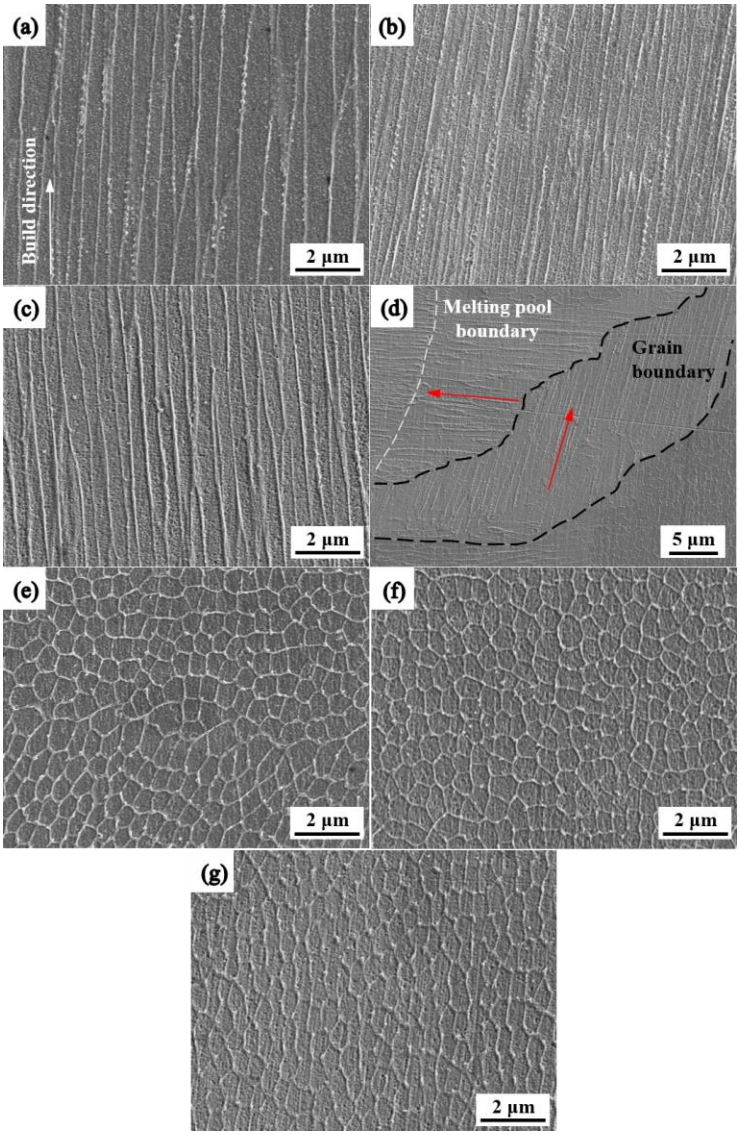

Figure 5: Higher magnification of microstructure.

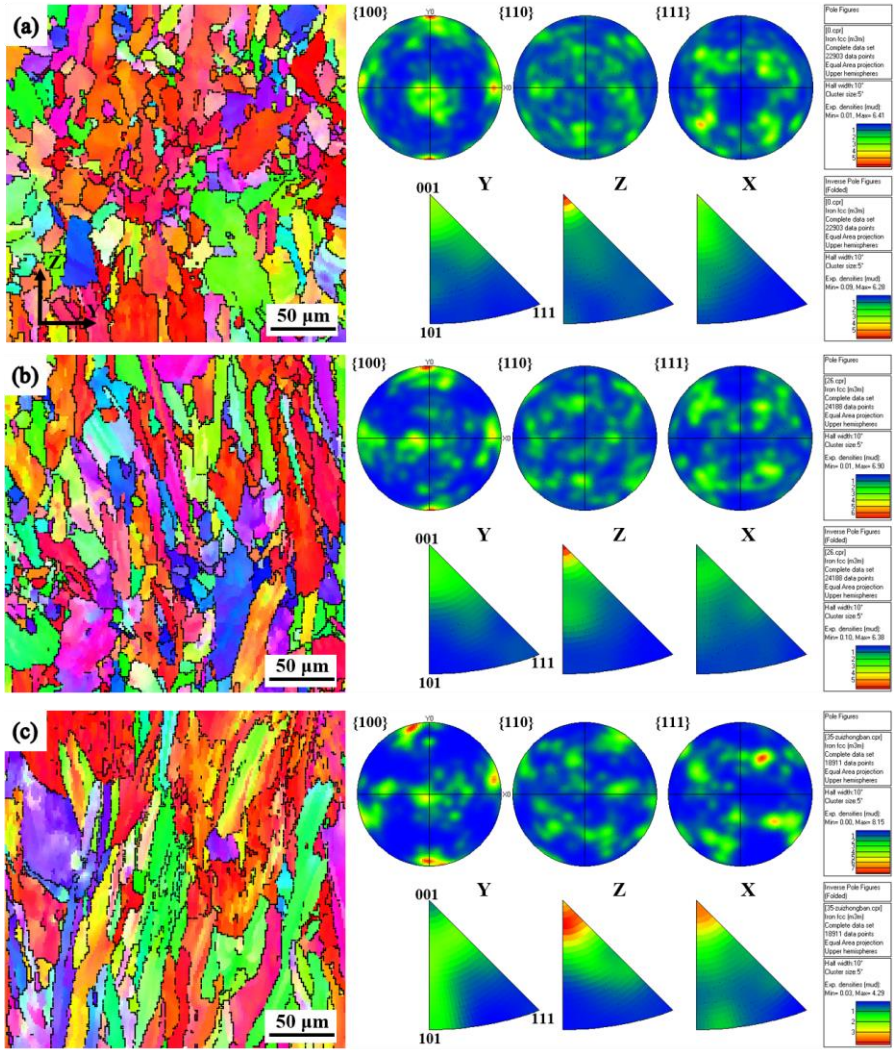

Figure 6: EBSD images.

3.2 Hardness

Figure 7 shows the hardness results of samples fabricated by three different scanning strategies. Sample A gives the lowest hardness value of 245±5 HV, which is similar to the hardness values obtained in previous studies listed in Table 2. Compared with the hardness of the sample A, the other two samples exhibit higher hardness, especially for the sample C which is over 280 HV. It indicates that the remelting strategies are beneficial to enhance hardness due to the higher energy input.

Table 2: Comparison of Vickers hardness obtained in previous studies.

Laser power (W)	Hatch space (μm)	Layer thickness (μm)	Exposure time (μs)	Point distance (μm)	Scanning speed (mm/s)	Energy density (J/mm³)	Hardness (HV)	Reference
200	80	40	80	65	812.5	77	244.5±2.3	Yang et al., (2019)
180	124	50	75	25	333	125	225	Cherry et al., (2015)
200	-	30	-	-	1600	-	250±16	Yusuf et al., (2018)
100	-	50	-	-	200	81	255±6	Kurzynowski et al., (2018)

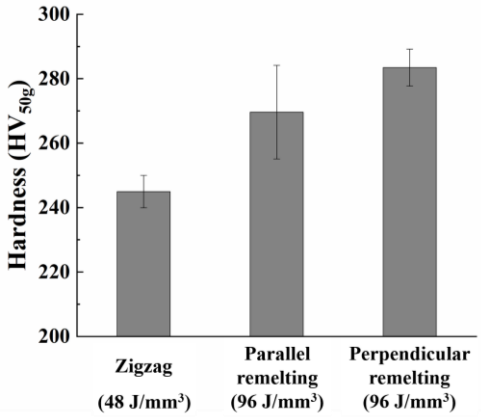

Figure 7: Hardness distribution.

3.3 Scratch Results

The scratch depths of all tracks are shown in Figure 8. Notably, the sample A gives the highest scratch depths while the lowest values corresponding to the sample C regardless of the applied loads. It should be pointed out that the significant decrease by more than 79 % in scratch depth is found under 1 N for the sample C compared with the sample A.

The morphologies corresponding to the scratch testing results are shown in Figure 8a-i. Under 1N, some debris and craters were observed on the edge of the scratch track on the sample A due to plowing, as shown in Figure 8a. Cracks were found in the centre of scratch track when the load increased to 3 N. The high load of 5 N results in severe damage. Local delamination, many craters and cracks were formed. The secondary plowing was also observed in the track, which was caused by the continuous sliding after the formation of wear debris. Compared with the sample A, the sample B showed the smooth scratch tracks under different loads. No cracks or craters were found in all tracks while only few debris and slight secondary plowing was seen under 3N and 5N. Similar conclusions apply for the sample C except for smaller track widths. The morphology of scratch tracks is well consistent with the results of scratch depths, which indicates the sample C has the highest wear resistance.

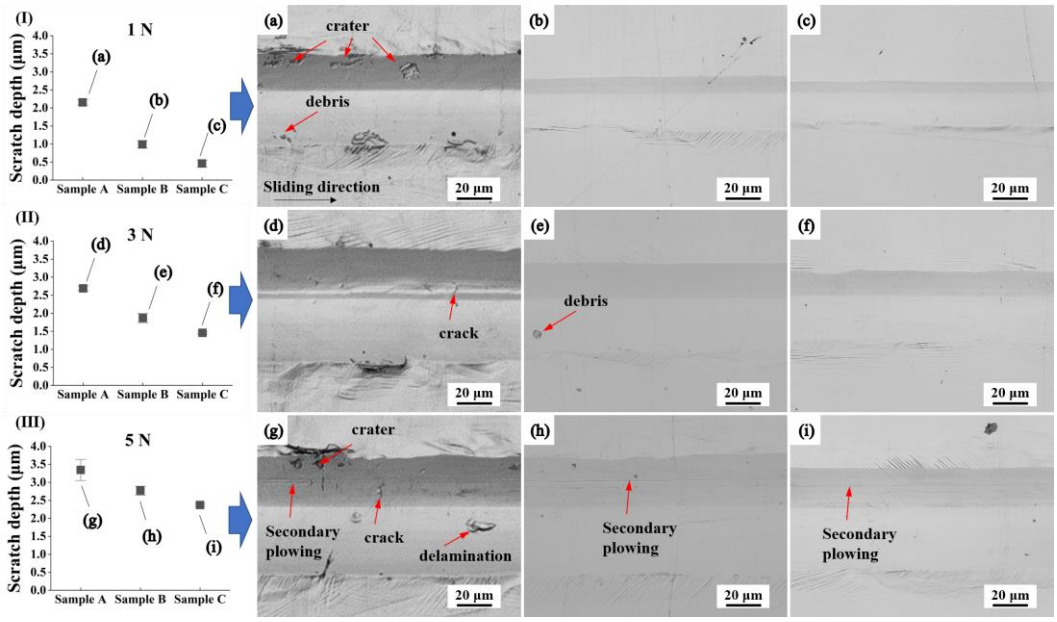

Figure 8: Scratch depth for all sample.

3.4 The Effect of Different Scanning Strategies On Wear Resistance

In SLM process, the fabricated materials were subjected to rapid heating and cooling cycles, which results in the formation of cellular and columnar structures/subgrains. When the remelting strategies were used, the high density of subgrain boundaries were created due to grain refining (Figure 5b and c). It indicates that the increase of subgrain boundaries has a great influence on the performance improvement due to the resistance of high degree dislocation. It significantly enhances the ability to resist deformation induced by the applied force. Therefore, the samples B and C exhibit higher wear resistance than the sample A, as illustrated in Figure 9.

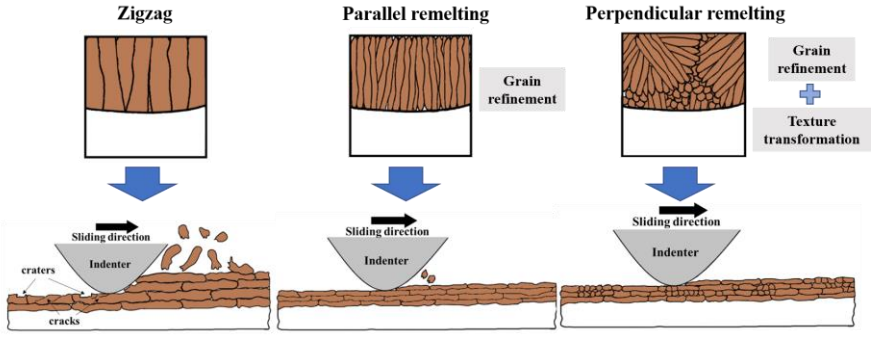

Figure 9: Wear mechanisms.

In generally, the solidification mode of materials was determined by the ratio of the temperature gradient G and growth rate R. With decreased G/R, the solidification modes changes from the planar to cellular, cellular-dendritic and, finally, dendritic solidification mode (Wang et al., 2016). Due to the high cooling rate (about 106 K/s) in SLM process (Wan et al., 2018), only

cellular solidification exists, which was observed in Fig. 5. During the solidification process, the grains grow perpendicularly to the molten pool boundary since the direction of maximum heat flux is always along with the normal of fusion lines (Yang et al., 2018). For the samples A and B, the main heat flux was generated in the build direction due to the unchanged scanning vectors in each layer, which can also be deduced from the approximately horizontal fusion lines in Fig. 4a and b. Given the fact that the <001> crystal direction is the preferred growth direction of a cubic metal, the strong <001> fibre texture aligned with the build direction was formed (Fig. 6a and b).

For the sample C, however, the heat flux direction changed with the rotation of scanning vectors. The crescent shape molten pool was produced by the remelting vectors along with X axis (Figure 4c). As shown in Figure 10, a radial heat flux (indicated by red arrows) occurs from the centre of molten pool to the boundary. As a result, the growth direction of cells in different location of the molten pool boundary are different. Moreover, the heat flux is usually influenced by the Marangoni flow and recoil pressure caused by the material evaporation (Wang et al., 2016; Qiu et al., 2015), which results in the formation of some small grains with random orientation (Figure 6c). In a conclusion, the <001> texture was greatly diminished, which is consistent with the weak <001> texture along with Z and X axis observed in Figure 6c. It should be noted that the weak <001> texture reduces the quality of columnar structures parallel to the sliding direction, which are more likely to slipping under the tangential force applied by the indenter (Yang et al., 2019). Therefore, the sample C shows the higher wear resistance than other two samples.

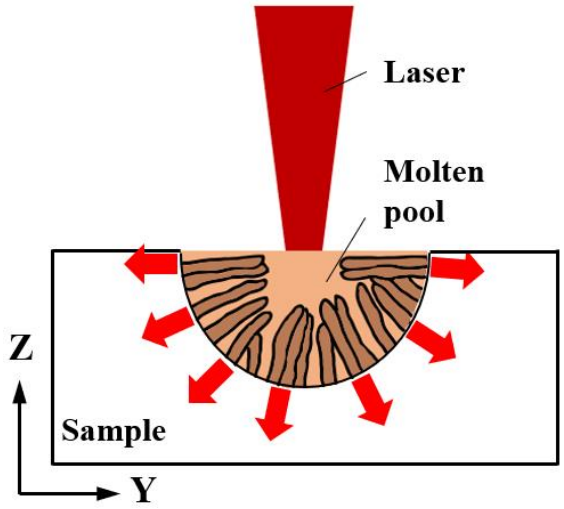

Figure 10: Heat flux formation.

4.0 CONCLUSION

Three types of scanning strategies were used to fabricate samples in this study. The microstructures were observed and the hardness was measured. The wear resistance of different samples was evaluated by scratch test. The conclusions can be draw as following:

(a) Remelting can enhance the hardness and wear resistance. The highest hardness of 283.5±6 HV and smallest scratch depth were obtained by using the perpendicular remelting strategy.

(b) The higher energy input by remelting leads to the refinement of microstructure resulting in the improved hardness and wear resistance.
(c) The fibre texture was reduced when the perpendicular remelting strategy was used, which enhance the wear resistance from a crystal texture view.

In this study, the influence of scanning strategies on the wear resistance was investigated, which suggests the high energy input by remelting can enhance hardness. However, the high energy input also can be realized using a low scanning speed or a large hatch space. The effects of changing different process parameters on microstructure and further on the properties of parts were unclear. On the other hand, the remelting process parameters also need to be studied in order to obtain a higher improvement on wear resistance.

ACKNOWLEDGEMENT

This work was supported by the National Key Research and Development Program of China [SQ2018YFB200029-04], National Natural Science Foundation of China [grant numbers 51775486 and 5189088].

REFERENCES

Zhu, Y., Zou, J., Chen, X., & Yang, H. (2016). Tribology of selective laser melting processed parts: Stainless steel 316 L under lubricated conditions. Wear, 350, 46-55.

Zhu, Y., Yang, Y., Lu, P., Ge, X., & Yang, H. (2019). Influence of surface pores on selective laser melted parts under lubricated contacts: a case study of a hydraulic spool valve. Virtual and Physical Prototyping, 14(4), 395-408.

Yang, Y., Zhu, Y., Khonsari, M. M., & Yang, H. (2019). Wear anisotropy of selective laser melted 316L stainless steel. Wear, 428, 376-386.

Lemke, J. N., Casati, R., Lecis, N., Andrianopoli, C., Varone, A., Montanari, R., & Vedani, M. (2018). Design of Wear-Resistant Austenitic Steels for Selective Laser Melting. Metallurgical and Materials Transactions A, 49(3), 962-971.

Cai, C., Radoslaw, C., Zhang, J., Yan, Q., Wen, S., Song, B., & Shi, Y. (2019). In-situ preparation and formation of TiB/Ti-6Al-4V nanocomposite via laser additive manufacturing: Microstructure evolution and tribological behavior. Powder technology, 342, 73-84.

Wen, S., Hu, H., Zhou, Y., Chen, Z., Wei, Q., & Shi, Y. (2018). Enhanced hardness and wear property of S136 mould steel with nano-TiB2 composites fabricated by selective laser melting method. Applied Surface Science, 457, 11-20.

J.H. Yi, J.W. Kang, T.J. Wang, X. Wang, Y.Y. Hu, T. Feng, Y.L. Feng, P.Y. Wu. (2019). Effect of laser energy density on the microstructure, mechanical properties, and deformation of Inconel 718 samples fabricated by selective laser melting. Journal of Alloys and Compounds, 786, 481-488.

Choi, J. P., Shin, G. H., Brochu, M., Kim, Y. J., Yang, S. S., Kim, K. T., ... & Yu, J. H. (2016). Densification behavior of 316L stainless steel parts fabricated by selective laser melting by variation in laser energy density. Materials Transactions, M2016284.

Qiu, C., Adkins, N. J., & Attallah, M. M. (2016). Selective laser melting of Invar 36: microstructure and properties. Acta Materialia, 103, 382-395.

Li, R., Shi, Y., Wang, Z., Wang, L., Liu, J., & Jiang, W. (2010). Densification behavior of gas and water atomized 316L stainless steel powder during selective laser melting. Applied surface science, 256(13), 4350-4356.

Wan, H. Y., Zhou, Z. J., Li, C. P., Chen, G. F., & Zhang, G. P. (2019). Effect of scanning strategy on mechanical properties of selective laser melted Inconel 718. Materials Science and Engineering: A, 753, 42-48.

Carter, L. N., Martin, C., Withers, P. J., & Attallah, M. M. (2014). The influence of the laser scan strategy on grain structure and cracking behaviour in SLM powder-bed fabricated nickel superalloy. Journal of Alloys and Compounds, 615, 338-347.

Thijs, L., Kempen, K., Kruth, J. P., & Van Humbeeck, J. (2013). Fine-structured aluminium products with controllable texture by selective laser melting of pre-alloyed AlSi10Mg powder. Acta Materialia, 61(5), 1809-1819.

Zhu, Y., Lin, G., Khonsari, M. M., Zhang, J., & Yang, H. (2018). Material characterization and lubricating behaviors of porous stainless steel fabricated by selective laser melting. Journal of Materials Processing Technology, 262, 41-52.

Zhu, Y., Zou, J., & Yang, H. Y. (2018). Wear performance of metal parts fabricated by selective laser melting: a literature review. Journal of Zhejiang University-Science A, 19(2), 95-110.

Yasa, E., Deckers, J., & Kruth, J. P. (2011). The investigation of the influence of laser re-melting on density, surface quality and microstructure of selective laser melting parts. Rapid Prototyping Journal, 17(5), 312-327.

Cherry, J. A., Davies, H. M., Mehmood, S., Lavery, N. P., Brown, S. G. R., & Sienz, J. (2015). Investigation into the effect of process parameters on microstructural and physical properties of 316L stainless steel parts by selective laser melting. The International Journal of Advanced Manufacturing Technology, 76(5-8), 869-879.

Yusuf, S. M., Nie, M., Chen, Y., Yang, S., & Gao, N. (2018). Microstructure and corrosion performance of 316L stainless steel fabricated by Selective Laser Melting and processed through high-pressure torsion. Journal of Alloys and Compounds, 763, 360-375.

Kurzynowski, T., Gruber, K., Stopyra, W., Kuźnicka, B., & Chlebus, E. (2018). Correlation between process parameters, microstructure and properties of 316 L stainless steel processed by selective laser melting. Materials Science and Engineering: A, 718, 64-73.

Wang, D., Song, C., Yang, Y., & Bai, Y. (2016). Investigation of crystal growth mechanism during selective laser melting and mechanical property characterization of 316L stainless steel parts. Materials & Design, 100, 291-299.

Wan, H. Y., Zhou, Z. J., Li, C. P., Chen, G. F., & Zhang, G. P. (2018). Effect of scanning strategy on grain structure and crystallographic texture of Inconel 718 processed by selective laser melting. Journal of materials science & technology, 34(10), 1799-1804.

Yang, H., Yang, J., Huang, W., Wang, Z., & Zeng, X. (2018). The printability, microstructure, crystallographic features and microhardness of selective laser melted Inconel 718 thin wall. Materials & Design, 156, 407-418.

Qiu, C., Panwisawas, C., Ward, M., Basoalto, H. C., Brooks, J. W., & Attallah, M. M. (2015). On the role of melt flow into the surface structure and porosity development during selective laser melting. Acta Materialia, 96, 72-79.